



Contents lists available at ScienceDirect

Physica D

journal homepage: www.elsevier.com/locate/physd

Effect of nonlinearity on the steady motion of a twinning dislocation

Anna Vainchtein

Department of Mathematics, University of Pittsburgh, Pittsburgh, PA 15260, United States

ARTICLE INFO

Article history:

Received 25 September 2009

Received in revised form

27 January 2010

Accepted 17 March 2010

Available online xxx

Communicated by K. Promislow

Keywords:

Twinning dislocation

Spinodal region

Kinetic relation

Velocity gaps

ABSTRACT

We consider the steady motion of a twinning dislocation in a Frenkel–Kontorova lattice with a double-well substrate potential that has a non-degenerate spinodal region. Semi-analytical traveling wave solutions are constructed for the piecewise quadratic potential, and their stability and further effects of nonlinearity are investigated numerically. We show that the width of the spinodal region and the nonlinearity of the potential have a significant effect on the dislocation kinetics, resulting in stable steady motion in some low-velocity intervals and lower propagation stress. We also conjecture that a stable steady propagation must correspond to an increasing portion of the kinetic relation between the applied stress and dislocation velocity.

© 2010 Elsevier B.V. All rights reserved.

1. Introduction

Martensites can accommodate very large deformations (up to 10% strain in ferromagnetic shape memory alloys) due to the phenomenon of twinning [1]. A planar twin boundary separates two symmetry-related variants of the same crystalline phase. When an external loading is applied, the atoms on one side of the twin boundary undergo a shear deformation relative to the other. On the microscopic level, a twin boundary propagates via the motion of twinning dislocations (also known as steps or ledges) along the boundary [2–4]. Lattice dynamics of a twinning dislocation thus largely determines the macroscopic kinetics of a twin boundary [5].

Since the mid-sixties, a lot of progress has been made in understanding dislocation dynamics on the lattice level (see [5–12] and the references therein, as well as [13,14] and other related work reviewed in [15]). Nevertheless, a number of questions remain open. In particular, existing lattice models generally predict that a dislocation cannot propagate steadily through an underdamped lattice with a velocity below a certain threshold. However, the influence of the nonlinearity of the elastic interactions on this threshold and on the existence and size of other “forbidden” velocity intervals is not well understood. This is the focus of this work.

To model the motion of a twinning dislocation, we use a variant of the well-known Frenkel–Kontorova (FK) model [16]. The model was originally formulated for slip dislocations in crystals but its various modifications have since been used to model a whole spectrum of physical and biological phenomena,

including twinning, dry friction, surface reconstruction, proton conductivity of hydrogen-bonded chains, the motion of domain walls in ferroelectrics, Josephson junctions and DNA dynamics and denaturation [15]. The model consists of a linearly elastic chain of particles placed in a nonlinear substrate potential. The linear nearest-neighbor interactions model interatomic interactions on the twin plane, and the nonlinear substrate potential accounts for the interactions with other atoms. In general, the substrate potential is periodic, with alternating slip and twinning energy barriers, but since in martensitic materials such as Cu–Al–Ni the energy barriers for slip are much higher than those for twinning [5], it suffices to consider a double-well potential. The wells correspond to two different variants of the martensite phase. A twinning dislocation is represented by a displacement profile that connects equilibrium states in two different wells. Under a force (representing an external loading of the crystal) applied to each particle, the dislocation is either pinned or propagates through the lattice. No internal damping is introduced, so the discrete system is Hamiltonian. Although the FK model is one-dimensional, it successfully captures the essential features of dislocation dynamics and is more transparent than its higher-dimensional counterparts.

A steadily moving dislocation is a traveling wave solution of the governing equations. As first shown by Atkinson and Cabrera in [6], exact analytical solution can be found for a two-parabola (biquadratic) substrate potential. In this case the nonlinearity is concentrated at one point where the two convex parabolae meet, and the traveling wave equation can be solved using Fourier transform. For smoother potentials, the existing literature mostly relies on the results of numerical simulations and continuum and active point approximations that are valid only within certain

E-mail address: aav4@pitt.edu.

velocity intervals and parameter regimes [11,17]. In this paper we consider a three-parabola substrate potential where the two convex parabolas (variant wells) are connected by a concave parabola that represents a non-degenerate spinodal region. Using the approach described in [12] in the context of a high-velocity screw dislocation motion, we find the traveling wave solution at a given velocity as a convolution of a certain shape function and the already available exact solution of the problem with a biquadratic potential. The shape function can be found by solving the eigenvalue problem for an integral operator whose kernel is again determined by the solution of the two-parabola problem. Recently this approach was used to analyze the role of spinodal region in a related quasilinear problem for a phase-transforming nonlinear chain [18]. In the context of FK model, some elements of this solution procedure were first introduced in [10], but the shape functions were only found using the continuum approximation and did not in general satisfy the consistency conditions of the discrete problem [12].

The constructed traveling wave profiles correspond to steady dislocation motion with speeds ranging from very small to supersonic. When velocity is smaller than a certain value, these solutions feature lattice waves of different wave lengths emitted both ahead and behind the moving dislocation. In contrast, Atkinson–Cabrera solutions for the biquadratic case exist only at relatively large velocities and have a single oscillation mode propagating behind the dislocation [6,11,17]. We show that the width of the spinodal region has a significant effect on the kinetic relation between the applied stress and the dislocation velocity. As in [12,18], we find that a wider spinodal region results in smaller amplitude of the lattice waves emitted by the moving front and a smaller driving force. When the spinodal region is sufficiently wide, the kinetic relation includes segments around certain selected speeds where the stress grows rapidly over a very small change in velocity. The fact that similar near-plateau segments at the same velocity values were observed numerically in [13] for FK model with sine nonlinearity suggests that this feature of dislocation kinetics does not depend on the details of the substrate potential as long as spinodal region is wide enough.

To verify the obtained solutions and study their stability, we conduct a series of numerical simulations of the initial value problem for the original discrete system. Using either piecewise constant displacement or the constructed solutions as initial conditions, we show that stable steady front motion may coexist with the equilibrium states (trapped dislocation) when the applied stress is below the Peierls value. Above the Peierls stress, there are no equilibrium states, and the numerical simulations converge to a stable steady front propagation. Since the numerical simulations only fall onto the increasing portions of the kinetic curve, we conjecture that this is a necessary (but not sufficient) condition for stability of steady dislocation motion. In the biquadratic case this is consistent with the hypothesis in [6] that only traveling waves above the minimum stress (called dynamic Peierls stress) of the highest-velocity kinetic segment are stable. As the width of the spinodal region is increased, propagation at lower velocity becomes stable. When the spinodal region is wide enough, there are two or more stable segments of the kinetic relation that correspond to different numbers of radiative modes emitted by the moving front. These segments are separated by velocity intervals where there is no stable steady motion. In some cases, a branch of non-steady states bifurcating from the obtained solutions may also become stable. In these solutions, which do not satisfy the traveling wave ansatz, propagation velocity oscillates about some average value.

To investigate the effect of full nonlinearity, we consider a one-parameter family of smooth functions that approximate the three-parabola potential. Numerical simulations with piecewise

constant initial data show similar stability results at the small value of the parameter. As we deviate further from the three-parabola potential, the lowest propagation speed becomes notably smaller and some other low-velocity solutions become stable. This suggests that strong nonlinearity plays a stabilizing role.

Overall, we find that nonlinearity in general and a sufficiently wide spinodal region in particular reveal a more complex structure of stable and unstable solutions of the FK model than the one suggested by the Atkinson–Cabrera solution for the biquadratic model. In particular, we show that a twinning dislocation can move steadily at speeds that are “forbidden” by this solution and emit waves in both directions. The combination of semi-analytical calculations and numerical simulations allows us to see features of the discrete kinetics, such as velocity gaps and the detailed structure of emitted lattice waves, that are easy to miss if one relies on numerical simulations alone.

The rest of the paper is organized as follows. The model is introduced in Section 2, and the traveling wave solutions for the three-parabola potential are constructed in Section 3. In Section 4 we discuss solution admissibility, obtain the kinetic relation and analyze its dependence on the width of the spinodal region. The equilibrium states are discussed in Section 5. In Section 6 we present the numerical simulations that suggest stability of some of the obtained solutions. The effect of nonlinearity is further analyzed in Section 7, and the concluding remarks can be found in Section 8.

2. The model

Consider an infinite Frenkel–Kontorova chain of particles of mass m connected by massless linear springs to each other and interacting with an external substrate potential $\Phi(u_n)$, where $u_n(t)$ is the displacement of the n th mass from its reference position at time t . We assume that the particles can move only along one direction and that an external stress σ , acting in the same direction, is applied to each mass. Let ϵ denote the reference length of the linear springs and $\rho = m/\epsilon$ be the mass density. The total energy of the system is given by

$$\mathcal{E} = \epsilon \sum_{n=-\infty}^{\infty} \left[\frac{1}{2} \rho \dot{u}_n^2 + \frac{1}{2} E \left(\frac{u_{n+1} - u_n}{\epsilon} \right)^2 + \Phi(u_n) - \sigma u_n \right],$$

and the equations of motion are

$$\rho \epsilon \ddot{u}_n - \frac{E}{\epsilon} (u_{n+1} - 2u_n + u_{n-1}) + \epsilon (\Phi'(u_n) - \sigma) = 0.$$

Here \dot{u}_n and \ddot{u}_n denote the first and second derivatives of $u_n(t)$, respectively, and $E > 0$ is the elastic modulus of the harmonic nearest-neighbor interactions. To model twinning, we assume that the substrate potential has two symmetric wells that represent two different variants of the martensite phase. The wells are located at $u = \pm a$ and have the local elastic modulus G :

$$\Phi'(\pm a) = 0, \quad G = \Phi''(\pm a) > 0.$$

We now introduce the dimensionless variables

$$\bar{t} = \frac{t}{\epsilon} \sqrt{\frac{\rho}{E}}, \quad \bar{u}_n = \frac{u_n}{a}, \quad \bar{\sigma} = \frac{\sigma}{aE}, \quad \bar{\Phi} = \frac{\Phi}{aE} \quad (1)$$

and the dimensionless parameter

$$\mu = \frac{G\epsilon^2}{E} \quad (2)$$

measuring the relative stiffness of the nonlinear interaction with the substrate. In terms of the new variables, with the bars dropped, the dimensionless equations of motion are

$$\ddot{u}_n = u_{n+1} - 2u_n + u_{n-1} + \mu(\sigma - \Phi'(u_n)). \quad (3)$$

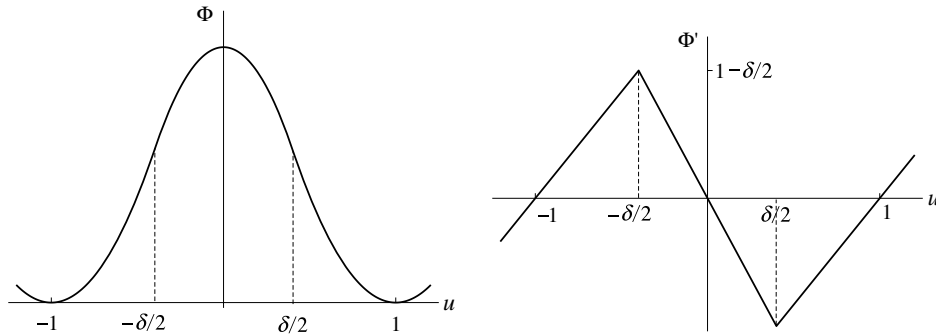


Fig. 1. The piecewise quadratic potential $\Phi(u)$ and its derivative (4).

To obtain semi-analytical results, we will further assume that the substrate potential is piecewise quadratic, with a continuous piecewise linear derivative

$$\Phi'(u) = \begin{cases} u + 1, & u < -\delta/2 \\ (1 - 2/\delta)u, & -\delta/2 \leq u \leq \delta/2 \\ u - 1, & u > \delta/2. \end{cases} \quad (4)$$

The two linearly increasing segments correspond to the two symmetric quadratic wells of $\Phi(u)$, connected by a downward parabola ($|u| < \delta/2$) that represents the *spinodal region* of width δ such that

$$0 \leq \delta < 2.$$

See Fig. 1.

3. Traveling wave solutions

To model a steadily moving twinning dislocation, we seek solutions of (3) in the form of a traveling wave:

$$u_n = u(\xi), \quad \xi = n - Vt. \quad (5)$$

Substituting this ansatz in (3), we obtain the advance-delay differential equation

$$V^2 u'' = u(\xi + 1) - 2u(\xi) + u(\xi - 1) + \mu(\sigma - \Phi'(u(\xi))). \quad (6)$$

In what follows, we will assume that $\Phi'(u)$ is given by (4). We are interested in finding solutions of (6) subject to the following conditions at infinity:

$$\langle u(\xi) \rangle \rightarrow \sigma \mp 1 \quad \text{as } \xi \rightarrow \pm\infty. \quad (7)$$

Here $\sigma \mp 1$ are stable equilibrium solutions of (6), and the angular brackets denote the average value of the displacement because we expect the Hamiltonian discrete system to develop oscillations. The average is taken over the largest oscillation period.

To solve the problem (6), (7) for given $V > 0$ and find the corresponding $\sigma = \sigma(V)$, we follow the approach of [12], which was recently applied to a related quasilinear problem in [18]. Since the details of the solution procedure can be found in [12,18], we only outline the main steps. First, we assume that $u(\xi)$ takes values inside the spinodal region ($|u| < \delta/2$) when ξ is in the interval $|\xi| < z$, for some $z > 0$ to be determined. We further assume that for $\xi < -z$ we have $u > \delta/2$ (second well) and for $\xi > z$ we have $u < -\delta/2$ (first well). Then we can write

$$\Phi'(u(\xi)) = u(\xi) - \int_{-z}^z h(s)(2\theta(s - \xi) - 1)ds, \quad (8)$$

where $\theta(s)$ is a unit step function, and we introduced an unknown shape function $h(s)$ which is zero outside the interval $[-z, z]$ and is normalized so that

$$\int_{-z}^z h(s)ds = 1 \quad (9)$$

Thus we obtain

$$V^2 u'' + (\mu + 2)u(\xi) - u(\xi + 1) - u(\xi - 1) = \mu \left[\sigma - 1 + 2 \int_{-z}^z h(s)\theta(s - \xi)ds \right]. \quad (10)$$

For consistency, we must require that in addition to (10) and (7), the solution satisfies the conditions

$$u(z) = -\frac{\delta}{2}, \quad u(-z) = \frac{\delta}{2} \quad (11)$$

and the inequalities

$$\begin{aligned} u(\xi) &> \frac{\delta}{2}, & \xi < -z \\ |u(\xi)| &< \frac{\delta}{2}, & |\xi| < z \\ u(\xi) &< -\frac{\delta}{2}, & \xi > z. \end{aligned} \quad (12)$$

Applying Fourier transform to (10) and using the convolution theorem, one can show (see [18] for details) that

$$\frac{du}{d\xi} = - \int_{-z}^z h(s)q(\xi - s)ds, \quad (13)$$

where the kernel is the negative derivative of the solution $u^0(\xi)$ of the problem with biquadratic potential with a degenerate spinodal region ($\delta = 0$) and $z = 0$:

$$q(\xi) = -\frac{du^0}{d\xi}. \quad (14)$$

At the same time, (4) and (8) imply that for $|\xi| < z$

$$\frac{d}{d\xi} \Phi'(u(\xi)) = \left(1 - \frac{2}{\delta}\right)u'(\xi) = u'(\xi) + 2h(\xi),$$

and thus $u'(\xi) = -\delta h(\xi)$ for $|\xi| < z$. Together with (13), this yields the integral equation

$$\int_{-z}^z h(s)q(\xi - s)ds = \delta h(\xi), \quad |\xi| < z. \quad (15)$$

Thus the shape function $h(\xi)$ is the eigenfunction of the integral operator in the left hand side of (15) with the kernel (14) associated with the eigenvalue δ . The eigenvalue problem is similar to the ones obtained in [12] for the uniform motion of a screw dislocation and in [18] for the motion of a phase boundary (with different kernels) and was derived in the same way.

The solution for any $\delta > 0$ is thus obtained from the solution $u^0(\xi)$ for the case of $\delta = 0$ (biquadratic potential) and $z = 0$. The latter can be found exactly using Fourier transform [6] (see also

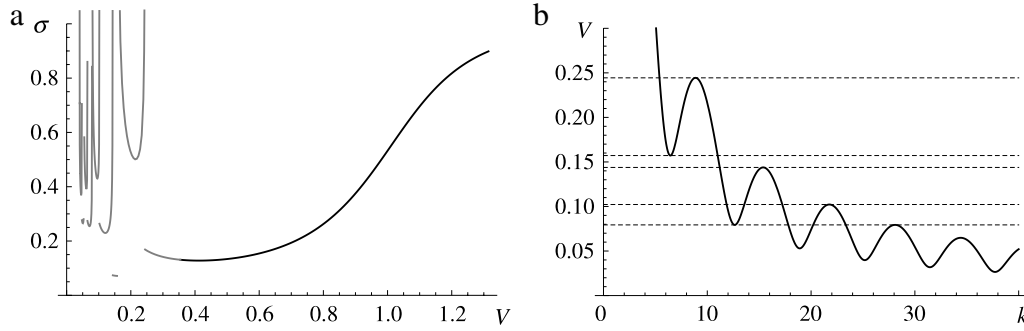


Fig. 2. (a) Kinetic relation resulting from the formally obtained Atkinson–Cabrera solution of the FK model with the biquadratic potential ($\delta = 0, z = 0$). Only the first twelve segments are shown. The grey curves correspond to inadmissible traveling waves. (b) Solutions of $L_k(k, V) = 0$ for positive real k . The dashed lines indicate the first five resonance velocities at which $L_k(k, V) = 0$. Here $\mu = 1$.

[11,17] for more details). Performing these calculations for our case, we obtain

$$u^0(\xi) = \begin{cases} \sigma^0 - 1 - 2\mu \sum_{k \in M^+(V)} \frac{e^{ik\xi}}{kL_k(k, V)}, & \xi > 0 \\ \sigma^0 + 1 + 2\mu \sum_{k \in M^-(V)} \frac{e^{ik\xi}}{kL_k(k, V)}, & \xi < 0, \end{cases} \quad (16)$$

where $L_k \equiv \partial L / \partial k$ and

$$\sigma^0 = 2\mu \sum_{k \in N(V)} \frac{1}{|kL_k(k, V)|}. \quad (17)$$

Here

$$M^\pm(V) = \{k : L(k, V) = 0, \text{Im } k \gtrless 0\} \cup N^\pm(V) \quad (18)$$

are the sets of roots of the dispersion relation

$$L(k, V) = \mu + 4 \sin^2 \frac{k}{2} - V^2 k^2 \quad (19)$$

contributing to the solution ahead (M^+) and behind (M^-) of the moving front, and

$$N^\pm(V) = \{k : L(k, V) = 0, \text{Im } k = 0, kL_k(k, V) \gtrless 0\} \quad (20)$$

denote the sets of real roots which correspond to lattice (phonon) waves emitted by the moving dislocation and are distributed according to the radiation condition [6,11]. This condition, also known as the causality principle [19], states that lattice waves can only be emitted by the moving front and must carry energy away from it (radiative damping). Thus phonon modes whose group velocity $V_g = V + L_k(k, V)/(2Vk)$ is less than velocity V of the front must be placed behind it (the set N^-), while the modes with group velocity above V propagate ahead (N^+). Note that the applied stress σ^0 in (17) is determined entirely by the real roots. As shown in [11], one can derive (17) by accounting for the energy fluxes carried by the phonon waves.

Knowing the solution (16) for a given $V > 0$, we determine the kernel of the integral operator in (15),

$$q(\xi) = \begin{cases} 2\mu i \sum_{k \in M^+(V)} \frac{e^{ik\xi}}{L_k(k, V)}, & \xi > 0 \\ -2\mu i \sum_{k \in M^-(V)} \frac{e^{ik\xi}}{L_k(k, V)}, & \xi < 0, \end{cases} \quad (21)$$

and find the unknown shape function $h(\xi)$ and its support $[-z, z]$ using a numerical approximation of (15), as described in the next section. The solution for $\delta > 0$ is then given by

$$u(\xi) = \sigma - \sigma^0 + \int_{-z}^z h(s)u^0(\xi - s)ds, \quad (22)$$

where the applied stress

$$\sigma = \sigma^0 - \frac{1}{2} \int_{-z}^z h(s)(u^0(z - s) + u^0(-z - s))ds \quad (23)$$

is found by using the switch conditions (11).

4. Admissible solutions and kinetic relations

Since the Atkinson–Cabrera solutions of the problem with biquadratic substrate potential ($\delta = 0, z = 0$) serve as the foundation for the construction of the traveling wave solutions in the case of a non-degenerate spinodal region, we start by briefly reviewing their properties. The reader is referred to [6,11,17] for additional details.

For each non-resonant velocity $V > 0$, one can calculate the traveling wave solution (16) and compute the corresponding applied stress σ using (17). The resulting functional relation $\sigma = \sigma(V)$, often referred to as a *kinetic relation*, is shown in Fig. 2a for the case of $\mu = 1$. The relation consists of disjoint segments separated by *resonance velocities*, i.e. values of V such that $L(k, V) = 0$ and $L_k(k, V) = 0$ for some real k (see Fig. 2b). A typical solution above the first resonance ($V = 0.5$) is shown in grey in Fig. 3.

One can see that a moving dislocation emits phonon oscillations behind it, with the wave number corresponding to the single real root of (19). As velocity decreases below the first resonance (see the grey curve at $V = 0.2$ in Fig. 3), more oscillation modes appear, and the formally obtained $u^0(\xi)$ features phonon emission on both sides. However, a closer inspection reveals that this “solution” is in fact inadmissible and should be removed because it violates the assumption that $u^0(\xi) < 0$ for $\xi > 0$. In fact, all segments of the kinetic relation below the first resonance do not contain any admissible traveling waves and thus need to be removed, while the remaining large-velocity segment contains admissible solutions above a certain threshold velocity [11] (in the case of $\mu = 1$, $V \geq 0.36$). This implies non-existence of traveling wave solutions with the velocity lower than the threshold value in the $\delta = 0, z = 0$ case. Nevertheless, as we will see, solutions that are non-admissible in this case still play an important role because they are used to construct admissible low-velocity solutions when $z > 0$.

Consider now potentials with $\delta > 0$. The procedure used to find the traveling wave solutions and obtain the kinetic relations in this case is as follows. After computing the kernel (14) of the integral operator in (15) from the solution (16) for a given V , the integral equation is approximated using the trapezoidal rule for a finite z , so that the eigenvalue problem reduces to finding z and \mathbf{h} such that the given δ is an eigenvalue of the resulting matrix in the numerical approximation, and the vector \mathbf{h} is the corresponding eigenvector that approximates the eigenfunction $h(\xi)$. In general, there is more than one value of z but our calculations show that at most one value

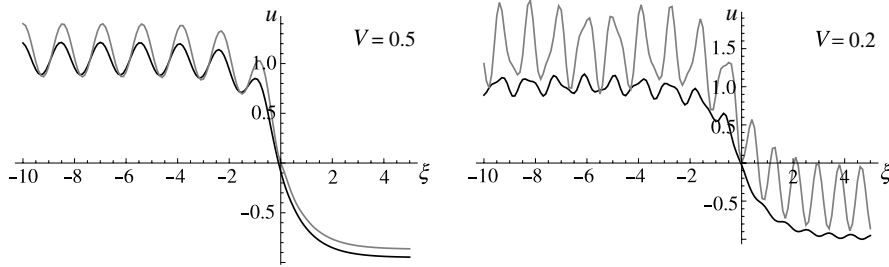


Fig. 3. Displacement profiles at $\delta = 0, z = 0$ (grey curves) and $\delta = 0.8$ with the corresponding nonzero z (black). At $\delta = 0, z = 0$ the traveling wave solution at $V = 0.5$ is admissible, while the one at $V = 0.2$ is not. At $\delta = 0.8$ both solutions are admissible. Here $\mu = 1$.

yields admissible solutions that satisfy the constraints (12). Once z and \mathbf{h} are found, the trapezoidal approximation of the integrals in (22) and (23) is used to compute the solution $u(\xi)$ and the applied stress σ .

The resulting displacement profiles at $\delta = 0.8$ are shown by black curves in Fig. 3. The main effects of $\delta > 0$ are the phase shift, the decreased amplitude of the oscillations and the lower value of the applied stress. These were also observed and explained in [12]. The phase shift occurs due to the continuous particle acceleration at $\delta > 0$ (as opposed to the discontinuity at $t = n/V$ when $\delta = 0$), which results in lower velocities and thus longer time needed to reach the maxima of oscillations. Meanwhile, wave modulation during the finite time interval $[n - z/V, n + z/V]$ when $\Phi'(u_n)$ for the well-switching n th particle has the negative slope leads to the diminished contribution of the short-wave oscillations to the energy radiation (and thus lower applied stress).

As a result of the smaller wave amplitude, velocities for which solutions were inadmissible at $\delta = 0$ and $z = 0$ may in fact lead to admissible solutions at sufficiently large $z > 0$. For example, the solution at $V = 0.2$ is admissible at $\delta = 0.8$, while the corresponding Atkinson–Cabrera solution for the biquadratic potential is not; see Fig. 3.

Fig. 4(a) shows the half-width z of the transition region as the function of V for $\delta = 0.4, 0.8$ and 1.2 . One can see that z increases with δ , as expected. The corresponding kinetic relations are shown in Fig. 4b. Remarkably, all solutions shown except the ones along the grey portions of the curves are admissible, i.e. satisfy the constraints (12). This includes solutions in the immediate vicinity of the resonance velocities which correspond to cusps in the figure.

As V tends to infinity, the kinetic relation approaches the spinodal value $\sigma_s = 1 - \delta/2$, the maximum value for which there exist equilibrium solutions of $\Phi'(u) = \sigma$ in two different wells. Thus z tends to infinity in this limit. We remark that at sufficiently large velocities (e.g. $V > 1.045$ at $\delta = 0.8$) the amplitude of the waves propagating behind becomes so large that the oscillations enter the spinodal region, violating the constraint $u(\xi) > \delta/2$ at $\xi < -z$ that was assumed to obtain solutions. The corresponding solutions are thus not admissible (see the grey large-velocity segments in Fig. 4), although, as we will see, they still predict the velocity of the front propagation obtained numerically. No admissible solutions were also found in the velocity interval $[0.163, 0.165]$ at $\delta = 1.2$ due to a small oscillation near the dislocation front (note the jump in the z value in Fig. 4a).

5. Lattice trapping and the Peierls threshold

In addition to dynamic solutions, there are trapped equilibrium states ($V = 0$) governed by the system of difference equations

$$u_{n+1} - 2u_n + u_{n-1} + \mu(\sigma - \Phi'(u_n)) = 0. \quad (24)$$

Solutions of (24) can be found, for example, in [20]. Here we merely summarize the results for completeness using our notation.

If no particles have displacement in the spinodal region, the problem is solved the same way as in the case of biquadratic potential considered in [21]. The equilibrium solutions with a single dislocation that has larger displacement behind are given by

$$u_n = \begin{cases} \sigma - 1 + Ay_2^n, & n \geq 0 \\ \sigma + 1 + (A - 2)y_1^n, & n < 0, \end{cases} \quad (25)$$

with

$$A = \frac{\sqrt{4 + \mu} - \sqrt{\mu}}{\sqrt{4 + \mu}}$$

and

$$y_{1,2} = 1 + \frac{\mu}{2} \pm \frac{\sqrt{\mu}}{2} \sqrt{4 + \mu}.$$

Solutions (25) exist if and only if the applied stress is inside the trapping region $|\sigma| \leq \sigma_p$, where

$$\sigma_p = \frac{\sqrt{\mu}}{\sqrt{4 + \mu}} - \frac{\delta}{2} \quad (26)$$

is the Peierls stress. At stresses outside the trapping region only dynamic solutions exist. Since the Peierls stress must be nonnegative, the obtained equilibrium solutions only exist for sufficiently narrow spinodal regions, i.e. when

$$0 \leq \delta \leq \frac{2\sqrt{\mu}}{\sqrt{4 + \mu}}.$$

For larger δ , equilibria must have at least one particle with spinodal displacement. The trapped states in the case of a single particle in the spinodal region are again given by (25) but with

$$A = 1 + \frac{2\mu\sigma y_1}{\delta((2 + \mu)y_1 - 2) - 2\mu y_1},$$

and the Peierls stress becomes

$$\sigma_p = \frac{(1 - y_2 - \delta/2)(\delta((2 + \mu)y_1 - 2) - 2\mu y_1)}{2\mu(1 - y_1) + \delta((2 + \mu)y_1 - 2)}. \quad (27)$$

Notice that the dependence on δ is no longer linear, as it was for (26). These solutions exist whenever

$$\frac{2\sqrt{\mu}}{\sqrt{4 + \mu}} \leq \delta \leq \sqrt{\mu}(\sqrt{4 + \mu} - \sqrt{\mu}).$$

Fig. 5 shows the dependence of Peierls stress on the width δ of the spinodal region for the cases of zero and one spinodal particles. Note that there is no lattice trapping ($\sigma_p = 0$) at $\delta = 2\sqrt{\mu}/\sqrt{4 + \mu}$ and $\delta = \sqrt{\mu}(\sqrt{4 + \mu} - \sqrt{\mu})$. At $\delta > \sqrt{\mu}(\sqrt{4 + \mu} - \sqrt{\mu})$ we need to insert two particles in the spinodal region, then three, etc.

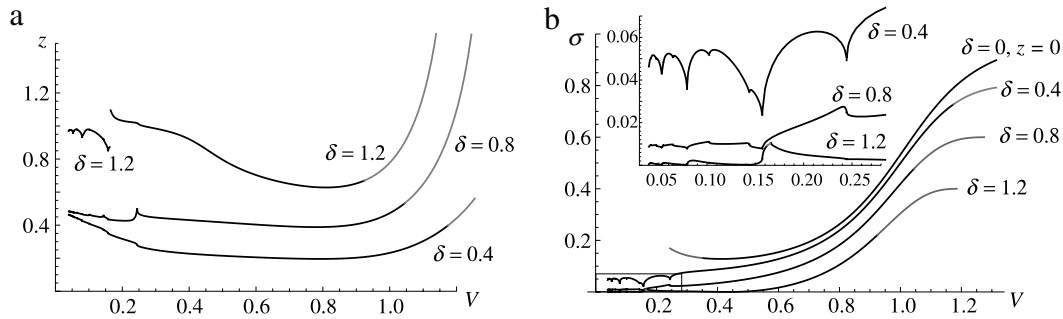


Fig. 4. (a) The half-width z of the transition region as the function of V for different δ and $\mu = 1$ calculated for $V \geq 0.04$. (b) The corresponding kinetic relations, shown together with the high-velocity segment at $\delta = 0, z = 0$. Inset: zoom-in of the small-velocity region. Grey portions indicate inadmissible solutions that violate the constraints (12).

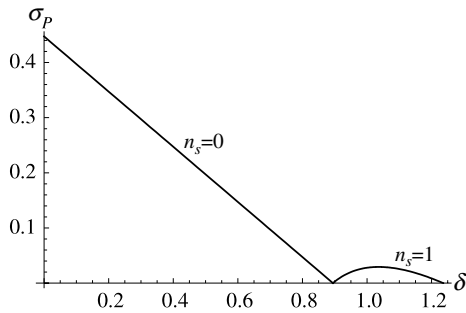


Fig. 5. Dependence of the Peierls stress on the width δ of the spinodal region at $\mu = 1$. Here n_s denotes the number of particles in the spinodal region in the corresponding trapped equilibria.

6. Stability of the traveling waves: numerical simulations

To investigate stability of the obtained traveling waves and verify the above calculations, we conducted a series of numerical simulations. For a given applied stress σ , we used the Verlet algorithm (a fourth-order symplectic scheme) to solve the system (3) of ordinary differential equation for a truncated lattice with N masses, ranging from $N = 600$ to $N = 2000$, depending on the time of the simulation. A longer chain was used if the simulation ran for a long time, in order to avoid reflection of elastic waves from the domain boundaries. The boundary conditions were $u_0 = \sigma + 1$ and $u_N = \sigma - 1$. Two types of initial conditions were used. The first one was Riemann-type piecewise constant initial displacement and zero initial velocity:

$$(u_n(0), \dot{u}_n(0)) = \begin{cases} (\sigma + 1, 0) & 0 \leq n < n_0 \\ (s, 0), & n = n_0, \\ (\sigma - 1, 0), & n_0 < n \leq N \end{cases} \quad (28)$$

where $0 \leq s < \delta/2$ and $n_0 = N/2$ for even N . Numerical simulations with this initial data sought to identify stable states at a given loading that have a relatively wide basin of attraction. Such tests would clearly miss other possibly stable states that coexist with solutions found using (28) but have a more narrow basin of attraction. To capture such states and identify solutions that are likely to be unstable, we used the second type of initial conditions that were built from the obtained traveling wave profiles $u_n(t) = u(n - Vt)$:

$$(u_n(0), \dot{u}_n(0)) = \begin{cases} (\sigma + 1, 0) & 0 \leq n < p \\ (u(n - n_0), -Vu'(n - n_0)) & p \leq n \leq N - p \\ (\sigma - 1, 0) & N - p < n \leq N. \end{cases} \quad (29)$$

The truncated traveling wave solutions were surrounded by intervals of constant displacement of appropriately chosen size $p < n_0$ in order to ensure compatibility with the boundary conditions and

avoid wave reflection from the boundaries. In both types of simulations, after a sufficiently long time (usually $t = 200$ but longer for small-velocity propagation), the solution approached an attractor corresponding to either a stationary dislocation (zero velocity) or a moving front. In most cases the front in the long-time solution propagated steadily, meaning that the time period during which the front moved from one lattice point to the next approached a constant value T , yielding the velocity $V = 1/T$. The velocity was averaged over the last ten periods.

Figs. 6–8 show the numerical results for $\delta = 0.4, 0.8$ and 1.2 , respectively, and compare them with the corresponding semi-analytical kinetic curves. Thick vertical segment along $V = 0$ axis indicates the trapping region $0 \leq \sigma \leq \sigma_p$ in each case. The results with piecewise constant initial conditions (28) are shown by black circles, while grey circles indicate the results with initial data (29) based on traveling wave solutions, with at least one solution taken from each decreasing or increasing portions of the kinetic curve. Numerical solutions corresponding to steady propagation (constant $V > 0$) fall onto the constructed kinetic curves. If the obtained velocity lies within the interval of admissible solutions, one can verify that the numerical solution near the front indeed approaches the corresponding traveling wave solution, indicating its stability. See, for example, Fig. 9, where the numerical solution at $\delta = 0.8$ that yields $V = 0.162$ is compared to the corresponding traveling wave solution. When $V = 0$, the long-time numerical solution near the front approaches the equilibrium state (25) for the given value of σ .

In all three cases shown in Figs. 6–8, stable steady motion coexists with a trapped state when σ is below the Peierls value. Above it, there are no equilibrium states, and the numerical results yield a steady front propagation. At $\delta = 0.4$ only the highest-velocity portion of the kinetic relation appears to contain stable steady motion; see the thicker black segment in Fig. 6. It corresponds to traveling wave solutions with a single oscillation mode that propagates behind the dislocation. In this case such solutions become stable at $V = 0.265$. At this value a branch of non-steady solutions bifurcates and becomes stable for $0.065 < \sigma < 0.069$. These solutions, shown by grey circles in Fig. 6b, were obtained using initial data (29) with corresponding traveling waves that have $V < 0.265$. Non-steady motion does not satisfy the traveling wave ansatz and thus is not captured by the constructed solutions. The non-steady states have velocity oscillating around the average value shown in the figure. The amplitude of velocity oscillations becomes smaller as the subcritical bifurcation point is approached. At $\sigma = 0.065$ and below the numerical simulations approach a trapped state. We conjecture that stability of the non-steady branch terminates at a turning point.

At larger values of δ non-steady motion was not observed. Instead, numerical simulations at $\delta = 0.8$ and $\delta = 1.2$ (see Figs. 7b and 8b) indicate that steady propagation can be stable at lower

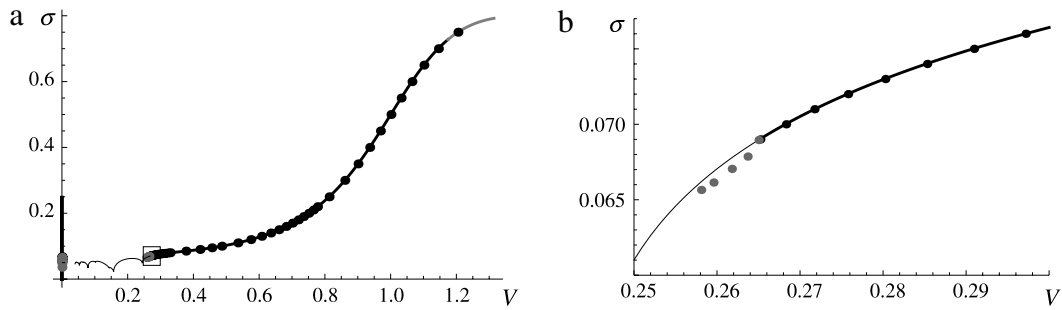


Fig. 6. (a) Results of the numerical simulations for $\delta = 0.4$ with initial data (28) with $s = 0.1$ (black circles) and (29) (grey circles), shown together with the kinetic curve. (b) Zoom-in inside the rectangle in part (a). Thicker black segments indicate stable solutions. Here $\mu = 1$.

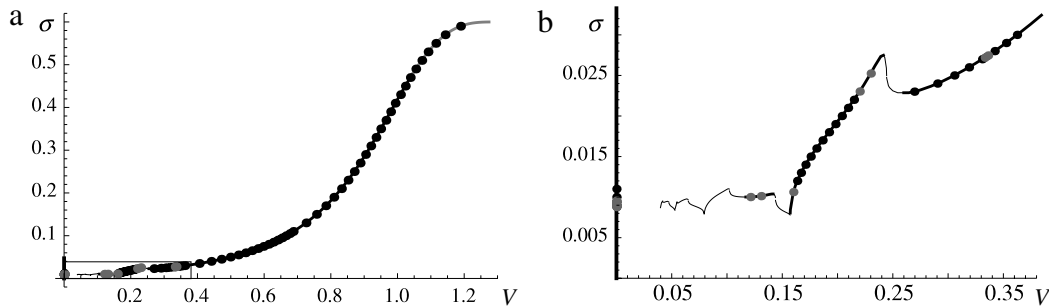


Fig. 7. (a) Results of the numerical simulations for $\delta = 0.8$ with initial data (28) with $s = 0.1$ (black circles) and (29) (grey circles), shown together with the kinetic curve. (b) Zoom-in inside the rectangle in part (a). Thicker black segments indicate stable solutions. Here $\mu = 1$.

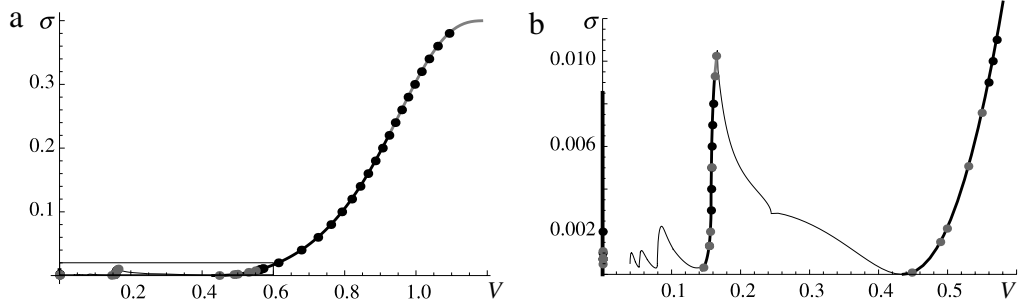


Fig. 8. (a) Results of the numerical simulations for $\delta = 1.2$ with initial data (28) with $s = 0.1$ (black circles) and (29) (grey circles), shown together with the kinetic curve. (b) Zoom-in inside the rectangle in part (a). Thicker black segments indicate stable solutions. Here $\mu = 1$.

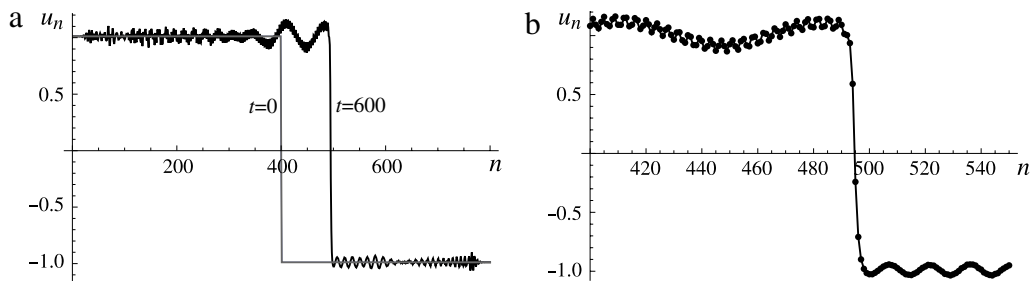


Fig. 9. (a) Displacement profiles (solid lines) at $t = 0$ and $t = 600$ for the numerical simulation at $\delta = 0.8$, $\mu = 1$ and $\sigma = 0.011$. (b) The numerical solution (dots) at $t = 600$ zoomed in around the dislocation front and compared to the traveling wave solution (solid curve) with the same velocity, $V = 0.162$.

velocities, along some segments of the kinetic relation (marked by thicker lines) that correspond to dislocation emitting lattice waves in both directions, as shown in Fig. 9. Note that stable solutions with different velocities may coexist at the same value of σ .

Overall, the numerical simulations suggest that a dislocation can move steadily through the lattice with velocities within certain preferred intervals separated by velocity gaps where there is no

stable steady motion. The structure of these gaps depends on the width of the spinodal region.

Observe that stable solutions fall onto some (but not all) portions of the kinetic curve where σ is increasing with V . Meanwhile, solutions along the parts where σ is decreasing appear to be unstable. For example, when the traveling wave with $V = 0.35$ at $\delta = 1.2$ is used in the initial condition (29), the numerical

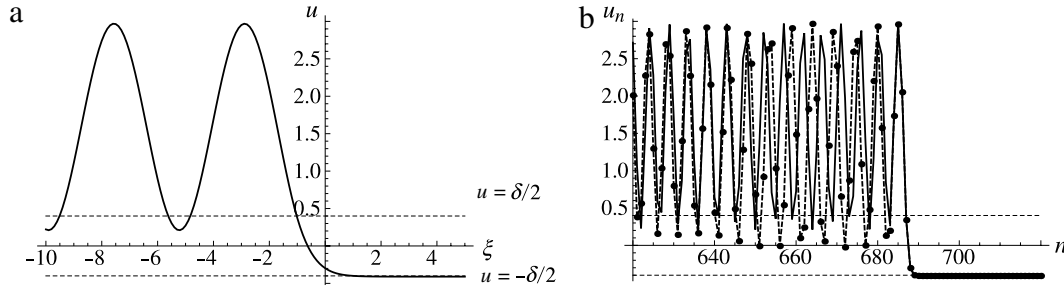


Fig. 10. (a) Inadmissible traveling wave profile at $V = 1.189$ ($\sigma = 0.59$) and $\delta = 0.8$ (b) Snapshot of the numerical solution (dots connected by dashed lines) at $t = 200$, with the same stress and velocity, zoomed in around the dislocation front and compared to the inadmissible traveling wave solution (solid curve).

solution around the front converges to the traveling wave with $V = 0.489$, which is located on the increasing portion of the kinetic segment at the same applied stress (see Fig. 8b). Similarly, starting from $V = 0.1$ at $\delta = 1.2$ leads to $V = 0.154$ on a stable segment. In general, our simulation results suggest the following

Conjecture. A necessary (but not sufficient) condition for stability of the traveling wave solution of (3) with velocity V is that it is located on the increasing portion of the kinetic curve: $\sigma'(V) > 0$.

We emphasize that the above condition is not sufficient. For example, at $\delta = 1.2$ the traveling wave solution with $V = 0.082$ is located along an increasing part of the kinetic curve (see Fig. 8b). Using it in the initial condition (29), however, we obtain the traveling wave with $V = 0.156$, on a stable segment. The necessity of the condition $\sigma'(V) > 0$ is suggested by the observation that velocity of each steady motion obtained via the numerical simulation corresponds to an increasing portion of the kinetic relation. Proving this conjecture is not an easy task even for the biquadratic problem. In this case a proof of stability of traveling waves with sufficiently high velocities can be found in [22], along with some remarks about extending these results to smoother potentials. Unfortunately, the proof does not extend to the entire conjectured stability interval, since it relies on positivity of Green's functions, and in the case of Hamiltonian lattice dynamics these functions change sign at speeds below a certain value [22].

Kinetic relation at $\delta = 1.2$ is particularly interesting because it contains nearly vertical segments around velocities $V = 0.1572$, $V = 0.0793$, $V = 0.0529$ and $V = 0.0398$. These are the resonance velocities corresponding to the first four local minima of the function $V = \hat{V}(k)$ obtained by solving equation $L(k, V) = 0$ for V (see Fig. 2b). Remarkably, segments of nearly constant velocity around the same speeds were also obtained in the numerical simulations in [13] for FK model with $\Phi'(u) = \sin u$, suggesting possible universality of this feature of the dislocation kinetics for substrate potentials with a sufficiently wide spinodal region. The difference is that in the present case only the segment near $V = 0.1572$ appears to be stable. This indicates that full nonlinearity may stabilize some of the lower-velocity solutions. This conjecture is supported by numerical results presented in Section 7.

We conclude this section with a remark about high-velocity solutions. Recall that at $\delta > 0$ traveling wave profiles with velocities above certain value (along the grey portions of the kinetic curves) are not admissible because the large-amplitude oscillations behind the front enter the spinodal region, violating (12); see Fig. 10a for an example. Nonetheless, these inadmissible portions of the kinetic curve give a very good prediction of the velocity of the steady motion at a given stress. For example, numerical simulation at $\sigma = 0.59$ yields steady motion at $V = 1.189$. Fig. 10b compares the corresponding inadmissible traveling wave “solution” (solid line), which also yields $\sigma = 0.59$, to the snapshot of the numerical simulation at $t = 200$ near the dislocation (dots connected by dashed

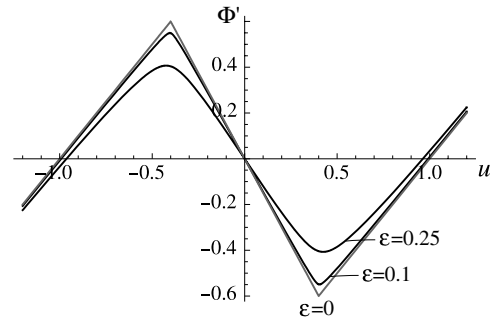


Fig. 11. The first derivative of the potential $\Phi_\varepsilon(u)$ defined in (30) for $\varepsilon = 0$ (grey curve) and $\varepsilon = 0.1$ and 0.25 (black curves). Here $\delta = 0.8$.

lines). The non-solution predicts the right velocity but there is a phase shift and amplitude difference in the oscillations behind the front, with numerical solution entering deeper inside the spinodal region. To capture the numerical solution in this case, one needs to appropriately modify the assumption (12).

7. Fully nonlinear potentials

In order to obtain semi-analytical solutions, we have assumed that the potential $\Phi(u)$ (for $\delta > 0$) has piecewise linear continuous first derivative and piecewise quadratic discontinuous second derivative. To investigate the effect of full nonlinearity on the Frenkel-Kontorova kinetics, for a given $\delta > 0$ we now consider a family of fully nonlinear potentials $\Phi_\varepsilon(u)$ with the second derivative given by

$$\Phi_\varepsilon''(u) = 1 - \frac{1}{\delta} + \frac{2}{\pi\delta} \arctan \frac{u^2 - \frac{\delta^2}{4}}{\varepsilon^2}. \quad (30)$$

In the limit $\varepsilon \rightarrow 0$ $\Phi_\varepsilon''(u)$ approaches the piecewise constant discontinuous second derivative $\Phi''(u)$ of the potential defined by (4). At small ε $\Phi'_\varepsilon(u)$ approximates the piecewise linear function $\Phi'(u)$ by smoothing its corners; see Fig. 11.

We conducted numerical simulations for fully nonlinear potentials with $\delta = 0.8$, $\varepsilon = 0.1$ and $\varepsilon = 0.25$ using piecewise constant initial conditions (28) with $s = 0.1$ and with $\sigma + 1$ and $\sigma - 1$ replaced u_l and u_r , respectively, where u_l, u_r are the equilibrium states located in the two wells: $\Phi'_\varepsilon(u_l) = \Phi'_\varepsilon(u_r) = \sigma$, $\Phi_\varepsilon''(u_l) > 0$, $\Phi_\varepsilon''(u_r) > 0$, $u_l > u_r$. The results of the simulations are shown in Fig. 12a, where the corresponding results for the piecewise linear case ($\varepsilon = 0$) are also included for comparison. At larger ε , the stress at a given velocity is lower, which is consistent with the lower spinodal stress. Otherwise, the results of the simulation at $\varepsilon = 0$ and $\varepsilon = 0.1$ are very similar in the sense that the velocity intervals corresponding to stable steady motion accessible

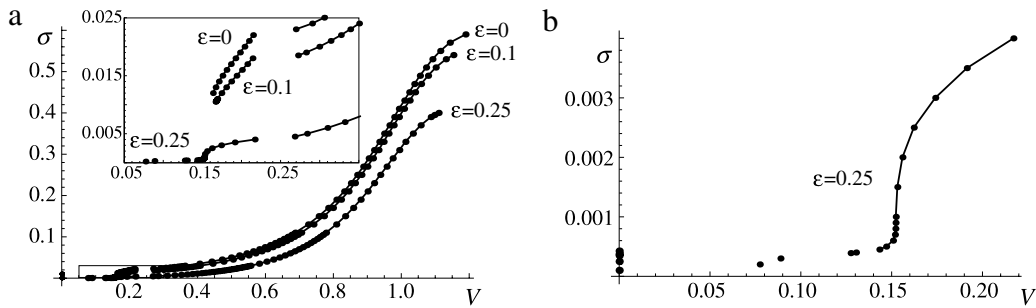


Fig. 12. (a) Results of simulations with piecewise constant initial conditions at $\varepsilon = 0$, $\varepsilon = 0.1$ and 0.25 . Insert zooms in on the rectangle near the origin. (b) Zoom-in of small-velocity region at $\varepsilon = 0.25$. Here $\delta = 0.8$ and $\mu = 1$.

from piecewise constant initial conditions are almost the same. However, at $\varepsilon = 0.25$ (strong nonlinearity) the lowest propagation speed, $V = 0.077$, is significantly smaller (see Fig. 12b). At $\varepsilon = 0$ this velocity belongs to the decreasing portion of the kinetic relation and the corresponding solution appears to be unstable (see Fig. 7b). Note also that the velocity interval $[0.143, 0.217]$ of apparently stable solutions at $\varepsilon = 0.25$ (see connected dots in Fig. 12b) includes velocities $0.143 \leq V \leq 0.157$ at which solutions at $\varepsilon = 0$ correspond to a decreasing part of the kinetic curve and are unstable (see Fig. 7b). The apparent stabilization cannot be attributed to the width of the spinodal region, which only slightly increases with ε . The results thus again suggest that the full nonlinearity plays a stabilizing role.

8. Concluding remarks

We studied the effect of nonlinearity of the elastic interaction potential on the motion of a twinning dislocation in the framework of FK model. Using a piecewise quadratic interaction potential with non-degenerate spinodal region, we constructed semi-analytical traveling wave solutions for a wide range of velocities. We showed that the width of the region has a significant effect on the kinetics of the dislocation and conducted numerical simulations to investigate stability of the obtained solutions. The simulations suggest that as the width of the spinodal region is increased, dislocation motion at some low speeds becomes stable. These solutions feature lattice waves emitted in both directions and may coexist with pinning and high-velocity propagation of the dislocation. We also found that steady motion may exchange stability with a branch of non-steady states bifurcating from the constructed solutions. We conjectured that a necessary condition for stability is that the solution is located on an increasing part of the kinetic relation. Our results show the existence of velocity gaps in which there is no stable steady motion. The size of these gaps depends on the width of the spinodal region. The gaps are completely eliminated only when unrealistically high internal damping is included into the model [10,21].

While more work is needed to understand the effect of full nonlinearity, our initial investigations suggest that it may further stabilize steady motion at low velocities. At the same time, the fact that a sufficiently wide spinodal region leads to a similar structure of low-velocity kinetics as observed in the simulations in [13] with sine nonlinearity indicates that this feature is determined by the width of the spinodal region and not the details of nonlinearity.

Although we presented our results in the context of twinning dislocations, the main conclusions apply more generally to a variety of physical and biological processes that can be described by the FK model or related higher-dimensional lattice models. To extend our calculations to a periodic potential one needs to impose additional constraints on the values of the displacement in

each well [21]. This will yield an upper bound for velocity beyond which the constructed solutions are no longer valid because the large amplitude of oscillations behind the front violates the constraints. However, the low-velocity behavior of solutions connecting two neighboring wells will remain the same. Of course, a periodic potential also makes possible solutions that connect non-neighboring wells (e.g. 4π -kinks [13]), and such solutions are clearly beyond the scope of this work.

Finally, we remark that while this work focused on potentials with non-degenerate spinodal region, the solution procedure may also be used to find admissible traveling wave solutions at low velocities in the case of biquadratic potential. This result will be presented elsewhere.

Acknowledgements

This work was supported by the NSF Grant DMS-0443928. The author thanks Phoebus Rosakis for inspiring discussions. Helpful comments by Ana Carpio and anonymous reviewers about the earlier version of this manuscript are gratefully acknowledged.

References

- [1] P. Müllner, V.A. Chernenko, G. Kostorz, Stress-induced twin rearrangement resulting in change of magnetization in a Ni-Mn-Ga ferromagnetic martensite, *Scr. Mater.* 49 (2003) 129–133.
- [2] D. Bray, J. Howe, High-resolution transmission electron microscopy investigation of the face-centered cubic/hexagonal close-packed martensite transformation in Co-31.8 Wt Pct Ni alloy: part I. Plate interfaces and growth ledges, *Metall. Mater. Trans. A* 27A (1996) 3362–3370.
- [3] J.P. Hirth, Ledges and dislocations in phase transformations, *Metall. Mater. Trans. A* 25A (1994) 1885–1894.
- [4] J.P. Hirth, J. Lothe, *Theory of Dislocations*, John Wiley and Sons, 1982.
- [5] R. Abeyaratne, S. Vedantam, A lattice-based model of the kinetics of twin boundary motion, *J. Mech. Phys. Solids* 51 (2003) 1675–1700.
- [6] W. Atkinson, N. Cabrera, Motion of a Frenkel-Kontorova dislocation in a one-dimensional crystal, *Phys. Rev. A* 138 (3) (1965) 763–766.
- [7] A. Carpio, L.L. Bonilla, Discrete models of dislocations and their motion in cubic crystals, *Phys. Rev. B* 71 (13) (2005) 134105.
- [8] V. Celli, N. Flytzanis, Motion of a screw dislocation in a crystal, *J. Appl. Phys.* 41 (11) (1970) 4443–4447.
- [9] S. Ishioka, Uniform motion of a screw dislocation in a lattice, *J. Phys. Soc. Japan* 30 (1971) 323–327.
- [10] S. Ishioka, Steady motion of a dislocation in a lattice, *J. Phys. Soc. Japan* 34 (1973) 462–468.
- [11] O. Kresse, L. Truskinovsky, Mobility of lattice defects: discrete and continuum approaches, *J. Mech. Phys. Solids* 51 (2003) 1305–1332.
- [12] N. Flytzanis, S. Crowley, V. Celli, High velocity dislocation motion and interatomic force law, *J. Phys. Chem. Solids* 38 (1977) 539–552.
- [13] M. Peyrard, M.D. Kruskal, Kink dynamics in the highly discrete sine-Gordon system, *Physica D* 14 (1984) 88–102.
- [14] R. Boesch, C.R. Willis, M. El-Batanouny, Spontaneous emission of radiation from a discrete sine-Gordon kink, *Phys. Rev. B* 40 (1989) 2284–2296.
- [15] O.M. Braun, Y.S. Kivshar, *The Frenkel-Kontorova model: concepts, methods and applications*, in: *Texts and Monographs in Physics*, Springer-Verlag, Berlin Heidelberg, 2004.
- [16] J. Frenkel, T. Kontorova, On the theory of plastic deformation and twinning, *Proc. Z. Sowj.* 13 (1938) 1–10.

- [17] A. Carpio, L.L. Bonilla, Oscillatory wave fronts in chains of coupled nonlinear oscillators, *Phys. Rev. E* 67 (2003) 056621.
- [18] A. Vainchtein, The role of spinodal region in the kinetics of lattice phase transitions, *J. Mech. Phys. Solids* 58 (2) (2010) 227–240.
- [19] L.I. Slepyan, *Models and Phenomena in Fracture Mechanics*, Springer-Verlag, New York, 2002.
- [20] J.H. Weiner, W.T. Sanders, Peierls stress and creep in a linear chain, *Phys. Rev.* 134 (4A) (1964) 1007–1015.
- [21] O. Kresse, *Lattice models of propagating defects*, Ph.D. Thesis, University of Minnesota, Minneapolis, MN 2002.
- [22] A. Carpio, Nonlinear stability of oscillatory wave fronts in chains of coupled oscillators, *Phys. Rev. E* 69 (2004) 046601.